GEOPHYSICS, VOL. 71, NO. 6 (NOVEMBER-DECEMBER 2006); P. B241–B256, 17 FIGS., 1 TABLE.
10.1190/1.2338823

Case History

Characterizing an unstable mountain slope using shallow 2D and 3D seismic tomography

Björn Heincke[1], Hansruedi Maurer[2], Alan G. Green[2], Heike Willenberg[3], Tom Spillmann[2], and Luigi Burlini[3]

ABSTRACT

As transport routes and population centers in mountainous areas expand, risks associated with rockfalls and rockslides grow at an alarming rate. As a consequence, there is an urgent need to delineate mountain slopes susceptible to catastrophic collapse in a safe and noninvasive manner. For this purpose, we have developed a 3D tomographic seismic refraction technique and applied it to an unstable alpine mountain slope, a significant segment of which is moving at 0.01–0.02 m/year toward the adjacent valley floor. First arrivals recorded across an extensive region of the exposed gneissic rock mass have extraordinarily low apparent velocities at short (0.2 m) to long (>100 m) shot-receiver offsets. Inversion of the first-arrival traveltimes produces a 3D tomogram that reveals the presence of a huge volume of very-low-quality rock with ultralow to very low P-wave velocities of 500–2700 m/s. These values are astonishingly low compared to the average horizontal P-wave velocity of 5400 m/s determined from laboratory analyses of intact rocks collected at the investigation site. The extremely low field velocities likely result from the ubiquitous presence of dry cracks, fracture zones, and faults on a wide variety of scales. They extend to more than 35 m depth over a 200 × 150-m area that encompasses the mobile segment of the mountain slope, which is transected by a number of actively opening fracture zones and faults, and a large part of the adjacent stationary slope. Although hazards related to the mobile segment have been recognized since the last major rockslides affected the mountain in 1991, those related to the adjacent low-quality stationary rock mass have not.

INTRODUCTION

Unstable mountain slopes are a serious hazard in populated regions of many countries (Crozier and Glade, 2005). As examples, the 1806 Goldau (Heim, 1932), 1881 Elm (Cooke and Doornkamp, 1990), 1963 Vajont (Müller, 1968), and 1987 Val Pola (Govi et al., 2002) rockfalls and rockslides caused heavy damage and numerous fatalities in the Swiss and Italian Alps. The 1903 Frank rockslide in the Canadian Cordillera was equally disastrous (Gerrard, 1988), and the 1970 Huascarán event (Plafker et al., 1971) in the Peruvian Andes was the planet's most catastrophic movement of rock and ice. Rapid population growth in mountainous regions and global warming with its associated increases in the number of exceptional weather events are likely to exacerbate the risk of devastating rock failures (Bader and Kunz, 1998). Accordingly, there is a need to implement suitable mitigation measures in the form of early warning systems and protective barriers. To design effective barriers, comprehensive knowledge of the locations and volumes of unstable rock is essential.

Landslides, the displacements of which are concentrated along distinct sliding planes, can usually be characterized with the help of

Manuscript received by the Editor July 7, 2005; revised manuscript received March 26, 2006; published online November 3, 2006; corrected version published online November 7, 2006.
[1]Swiss Federal Institute of Technology, Institute of Geophysics, ETH-Hönggerberg, CH-8093, Zürich, Switzerland and IFM-GEOMAR Wischhofstrasse 1-3, D-24148 Kiel, Germany. E-mail: bheincke@ifm-geomar.de.
[2]Swiss Federal Institute of Technology, Institute of Geophysics, ETH-Hönggerberg, CH-8093, Zürich, Switzerland. E-mail: maurer@aug.ig.erdw.ethz.cl; alan@aug.ig.erdw.ethz.cl.
[3]Swiss Federal Institute of Technology, Geological Institute, ETH-Hönggerberg, CH-8093, Zürich, Switzerland.

standard 2D geophysical techniques (McCann and Forster, 1999; Hack, 2000). Results of determining the geometries of the failure planes and volumes of unstable rock based on isolated or relatively sparse 2D profiles are reported by Bruno and Marillier (2000; seismic reflection, electromagnetic, self-potential), Cummings (2000; electromagnetic), Havenith et al. (2000; refraction and geoelectric), Jongmans et al. (2000; refraction and geoelectric), Schmutz et al. (2000; geoelectric and electromagnetic), and Lapenna et al. (2005; geoelectric).

For highly fractured unstable crystalline rock without dominant sliding planes, the internal processes responsible for catastrophic rock failure are complicated (Hudson, 1992; Erismann and Abele, 2001; Eberhardt et al., 2001). Because movements of crystalline rock may be unevenly distributed over numerous discrete blocks, information on the block-bounding fracture and fault networks is crucial for understanding slope instabilities and for estimating unstable rock volumes (Willenberg, 2004). The inherent 3D nature of unstable crystalline rock usually makes the application of sparse 2D geophysical profiling techniques unsuitable, such that the characterization of the slope instabilities are often based on the results of geological mapping, sparse borehole measurements, geodetic observations, and the extrapolation of data provided by one or more of these three methods. These approaches are likely to supply only limited knowledge of the geology and mechanical properties of the subsurface. To address this issue, high-resolution geophysical techniques for the comprehensive volume surveying of unstable mountain slopes distinguished by rugged terrains are required (Dussauge-Peisser et al., 2003).

We have developed a 3D tomographic seismic refraction technique and employed it for determining the P-wave velocity structure of a highly fractured mountain slope close to the village of Randa in the Matter Valley of Switzerland (Figure 1). Similar 3D tomographic techniques have been applied in investigations of colluvial wedges along seismically active faults (Morey and Schuster, 1999), regions of archaeological interest (Polymenakos et al., 2004), and a fractured granitic body (Martí et al., 2002). Although the tomographic images of Martí et al. (2002) did not resolve individual fractures, they did identify regions of low seismic velocity that outlined zones of altered rock associated with the fractures.

After reviewing briefly the rockfall history, geology, and other critical data related to the Randa investigation site, we describe a simple seismic-velocity-based scheme for classifying rock quality. We then present our seismic data acquisition strategy and tomographic inversion techniques. Important information on the velocity structure beneath the unstable mountain slope is provided by the 2D and 3D tomograms, but only the 3D tomogram provides a fully consistent pattern of subsurface velocities at the crossover points of the 2D profiles and details on the lateral extent of certain key features. Finally, we suggest that a broad zone of ultralow to very low P-wave velocities probably defines a highly fractured region of rock that extends well beyond the boundaries of unstable rock inferred from surface geological mapping and geodetic observations.

RANDA INVESTIGATION SITE

Two major rockfalls in the spring of 1991 resulted in the dislocation of 30 million m^3 of crystalline rock and the formation of a steep-sided debris cone (Figure 1) that destroyed several holiday apartments and barns close to the village of Randa and blocked the main road and railway track connecting the Rhône Valley to the major tourist resort of Zermatt (Schindler et al., 1993; Satori et al., 2003). Damming of the Mattervispa River by the debris cone led to flooding in upstream regions of the valley, including parts of Randa. Fortunately, there were no fatalities. Continued displacements at numerous fracture zones and faults suggest that 2.7–9.2 million m^3 of the remaining rock mass is moving slowly to the southeast (Figure 2; Eberhardt et al., 2001; Jaboyedoff et al., 2004; Willenberg, 2004).

Relevant research activities at Randa

A geodetic network (see black and blue dots that mark reflector locations in Figure 2) that provides estimates of absolute surface displacement was installed immediately after the 1991 rockfalls (Jaboyedoff et al., 2004), and over the past few years we have been involved in a multidisciplinary project aimed at improving our understanding of rock failure at Randa (Eberhardt et al., 2001). Three moderately deep boreholes (SB50N: 51.0 m deep; SB50S: 52.5 m deep; SB120: 120.8 m deep; blue dots in Figure 3) were drilled into blocks of relatively intact rock within the central part of the unstable slope. It is in this general region where the greatest surface displacements were observed. After geologically and geophysically logging the boreholes and conducting a variety of crosshole and hole-to-surface geophysical surveys, the boreholes were equipped with inclinometers, extensometers, time-domain reflectometry cables, and three-component (3-C) seismometers. Nine 3-C seismometers were also permanently installed at shallow depths (0.5–5.0 m deep)

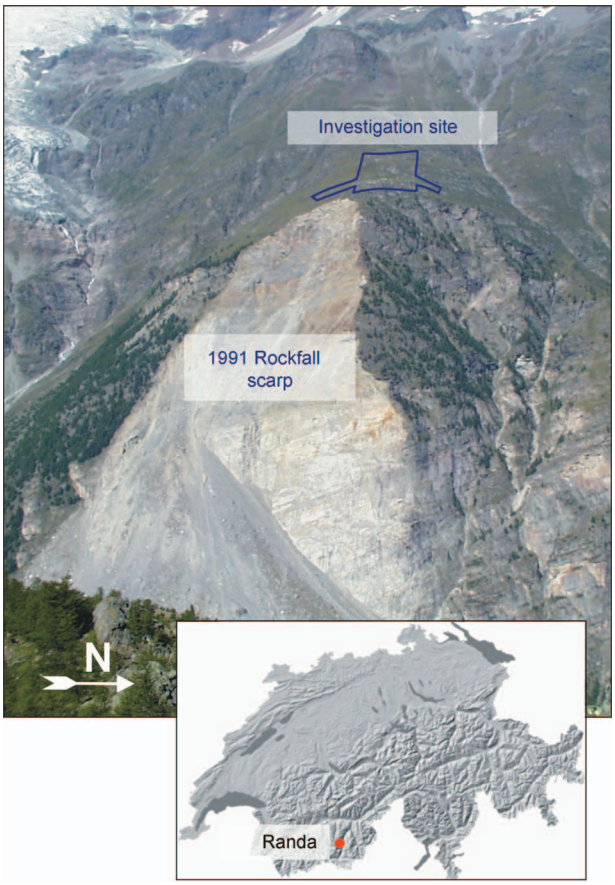

Figure 1. The investigation site is located on an unstable mountain slope above the scarp of the 1991 Randa rockfall in the Swiss Alps. Inset shows the location of Randa within Switzerland.

across the mountain slope (green dots in Figure 3). In addition to the geological mapping of Willenberg (2004), surface-based and cross-hole georadar measurements have provided details on the distribution of fracture zones and faults to depths as great as 30 m (Heincke et al., 2005a, b; Spillmann et al., 2006). P-wave seismic velocities of dry rock cores measured under varying hydrostatic pressures provided velocity estimates of the intact rock matrix.

Topographic relief

Our investigation site is situated about 50 m northwest of the 1991 rockfall scarp (Figure 1). It lies above the tree line at elevations of 2285–2450 m. The topography is extremely rugged, with various parts of the mountain slope dipping 20°–30° to the northeast, east, and southeast (Figures 2 and 3). Although crystalline rock is exposed at various locations across the site, some regions are covered by a thin layer of moraine and slope debris (maximum thickness of a few meters) and low-lying vegetation and pasture.

Rock lithologies and fracture/fault distribution

The geological map in Figure 2 is simplified from Willenberg (2004). It is based on the numerous rock outcrops, information derived from the three boreholes, and analyses of areal photographs. Three principal types of gneiss are recognized in the general area of the investigation site: (1) chloritic gneiss with schists, (2) medium-grained feldspar-rich gneiss with intercalations of so-called Randa augengneiss, and (3) heterogeneous gneiss. Their foliation dips west-southwest with an inclination of 20°–25°.

A network of open fracture zones and faults can be seen at outcrops above and on the rockfall scarp (Figure 2; Willenberg, 2004). In areas covered by moraine and debris, lineaments on areal photographs allow many of the fracture zones and faults to be interpolated or extrapolated over relatively long distances (e.g., 30 to several hundred meters). Three subsets of fracture zones and faults with different dominant orientations have been recognized (Willenberg, 2004); some of these were intersected by the boreholes. One subset dips at shallow angles to the southwest, parallel to the bedrock foliation. The other two are mostly steeply dipping (i.e., 25°–90°). One strikes north-south with easterly dips (e.g., B-E in Figure 2) and the other strikes northeast-southwest with northwesterly dips (e.g., A and F-L in Figure 2). It is the steeply dipping fracture zones and faults that likely define the instability of the mountain slope (Willenberg et al., 2002).

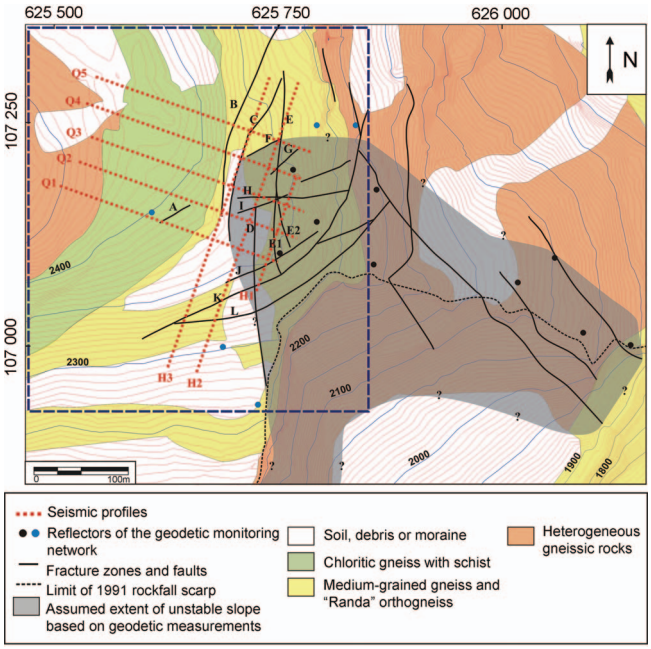

Figure 2. Geological map of the investigation site and its surroundings. Locations of the seismic profiles are shown by dashed red lines. Major surface fracture zones and faults and associated lineaments (A–L within the investigation site) are delineated by solid black lines. The 1991 rockfall scarp is outlined by the dashed black line and the lateral extent of the presently unstable rock mass according to Willenberg (2004) corresponds to the gray shaded area. Black dots show reflector positions of the long-term geodetic monitoring system that are moving, whereas the blue dots show reflector positions that are currently stationary. The digital elevation model (contours are meters above sea level) was provided by the Centre de Recherche sur l'Environment Alpin (CREALP). Expanded view of area outlined by the box (blue dashed lines) is shown in Figure 3.

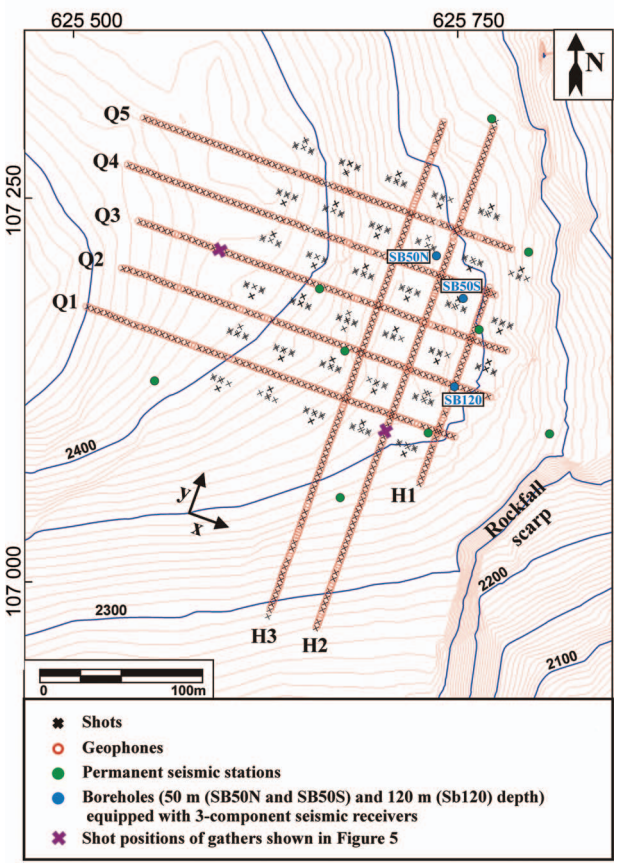

Figure 3. Geometry of the seismic survey. Black crosses and red circles show the source and receiver locations, which are mostly arranged along eight profiles approximately parallel (Q1–Q5) and perpendicular (H1–H3) to the mountain slope. Clusters of additional source locations are situated alongside the profiles. There are eight source locations per cluster (one for each profile). Green dots indicate the positions of nine permanent receivers deployed in shallow holes. Blue dots identify receivers deployed in boreholes SB50N, SB50S, and SB120 at depths of 42.7 m, 43.2 m, and 113.0 m, respectively. Contours are meters above sea level. Shot gathers presented in Figure 5 were generated by shots located at the two purple crosses.

Movements of the rock mass

Repeat geodetic measurements demonstrate that the mountain slope close to the 1991 rockfall scarp is moving to the southeast at a maximum rate of 0.01–0.02 m/year, with values decreasing in a northwesterly direction (Figure 2; Jaboyedoff et al., 2004; Willenberg, 2004). The base of borehole SB120 is moving about 0.01 m/year faster than the top. Movements at the surface and in the boreholes appear to be localized across active fracture zones and faults with opening rates of 0.001–0.003 m/year.

Rock velocity measurements

Samples of unfractured rock from 15 large-diameter cores retrieved from shallow boreholes at Randa were subjected to P-wave velocity analyses in the laboratory using Burlini et al.'s (2005) modifications to the original technique introduced by Birch (1960). Three small-diameter cores were extracted from each large core: one parallel to the foliation in the downdip direction (x_1), one parallel to the foliation in the strike direction (x_2), and one perpendicular to the foliation (x_3). Average velocities of core samples under atmospheric pressures were relatively low, ranging from 4900 m/s (x_1-oriented cores) through 4300 m/s (x_2-oriented cores) to 2600 m/s (x_3-oriented cores). The lowest values in the x_1/x_2 and x_3-directions were 3000 m/s and 1300 m/s, respectively. Velocities similar to those observed in the x_1/x_2-directions were recorded on sonic logs acquired at Randa (Spillmann et al., 2006).

It is well known that the core extraction process creates microfractures in the rock samples (Simmons et al., 1975), such that the unusually low velocities and associated high porosities may not be meaningful. Consequently, velocities of six suites of dry core samples were measured under increasing hydrostatic pressure conditions. At the lowest hydrostatic pressure of 20 MPa (equivalent to depths of 500–600 m), the average velocity of cores oriented in the x_1/x_2-directions increased to 5400 m/s and the average of cores oriented in the x_3-direction attained a value of 4700 m/s, corresponding to an average anisotropy of 13%. At 500 MPa, these average velocities increased to 6500 and 6100 m/s, representing a markedly decreased average anisotropy of only 6%. Our laboratory-determined velocities at atmospheric and higher pressures are within the range of gneissic rock velocities determined by Kopf (1977), Gebrande et al. (1982), and Jahns et al. (1994).

The relatively high velocities measured at pressures $\geq$20 MPa suggest that minerals in the near-surface rocks have not been greatly altered by weathering processes.

Table 1. Acquisition parameters used for the seismic survey.

Profile	Profile length (m)	Shot spacing (m)	Receiver spacing (m)	Number of inline shots	Number of inline receivers	Number of traces	Number of picks
H1	126	4	2	29	64	1856	1402
H2	324	4	2	77	up to 163	12,095	5217
H3	315	4	2	71	159	11,289	5582
Q1	238	4	2	57	120	6840	3102
Q2	238	4	2	57	120	6840	2805
Q3	238	4	2	55	120	6600	3940
Q4	238	4	2	59	120	7080	5012
Q5	238	4	2	59	120	7080	4008
		Offset shots		251		30,771	15,158
		Permanent receivers			12	8580	6374
		Total		715	998	99031	52,600
Areal extent of the investigation area:		250 × 250 m					
Recording systems:		Geometrics geodes					
Sampling rate:		0.8 ms					
Source type:		Dynamite					
Charges:		5–50 g					

SEISMIC ROCK QUALITY DESIGNATION (SRQD)

Various parameters are used to describe rock quality in civil and geotechnical engineering. One simple classification scheme based on borehole core analyses is the rock quality designation (RQD; Deere et al., 1967). Although RQD was introduced as a means to classify rock quality in tunneling applications, it is also used for studies of slope instabilities (Hack, 2000).

Observational data suggest that RQD can be related to field-based P-wave velocities V_{field} and laboratory-based velocity measurements of intact samples V_{lab} as follows (Deere et al., 1967; Hack, 2000):

$$\mathrm{SRQD} = \left(\frac{V_{\mathrm{field}}}{V_{\mathrm{lab}}}\right)^2 \times 100\%, \qquad (1)$$

where we use SRQD to emphasize that these RQD values are based on seismic velocities. For Randa, we set V_{lab} = 5400 m/s, the average velocity of dry core samples in the x_1/x_2-directions measured at 20 MPa hydrostatic pressure. To identify regions of ultra-poor (SRQD $<$8%) and very poor (SRQD 8%–25%) quality rock, we highlight ultralow ($<$1500 m/s) and very low (1500–2700 m/s) velocities in representations of our 3D tomogram.

DATA ACQUISITION

The seismic survey was designed to cover accessible parts of the unstable rock mass as determined by the geologic and geodetic data and large regions of the presumed stable mountain slope (Figures 2 and 3). The primary layout comprised eight profiles, of which five were parallel (Q1–Q5) and three were perpendicular (H1–H3) to the general downslope direction. Source and receiver spacings along the 126–324-m-long profiles were 4 and 2 m, respectively (Table 1). By using seven 24-channel Geode recording systems, we were able to deploy receivers along the entire length of each profile. To avoid damaging the sensitive high alpine environment and possibly increasing mountain slope instability, small shot charges of 5–50 g were detonated in shallow (0.5–0.7-m-deep) percussion-drilled holes. In addition to the shotholes along the profiles, we

also drilled clusters of eight holes (one per profile) at 33 locations offset from the profiles. Signals generated by shots detonated at these clusters were recorded on receivers along all profiles, thus providing a relatively high degree of 3D coverage (Figure 3). Furthermore, all inline and offset shots were recorded by the three deep borehole geophones and nine near-surface 3-C receivers. Together, the profiles and offset shots and receivers yielded moderately good to very good coverage of the entire investigation volume (Figure 4).

Because the site could not be accessed by motorized vehicles, equipment was transported from the valley floor to the investigation site by helicopter. Moreover, data acquisition was complicated by the rugged terrain; elevations varied by 50–125 m along the lengths of most profiles. A four-person crew required two months to acquire the data.

In the following, the origin of our coordinate system is the top of borehole SB120 (2356 m above sea level) and the x- and y-axes are parallel to the Q and H profiles, respectively.

DATA QUALITY

Because of the highly variable surface conditions and the small shot charges, the data quality ranges from poor to very good (see the typical shot gathers in Figure 5a and b and in Appendix B). Maximum offsets at which the first-arrival times can be unambiguously picked rarely exceed 200 m. In the shot gather of Figure 5b, the conspicuous loss of high frequencies and significant delay of first arrivals near $x = -51$ m are evidence for significant lateral and depth variations in the physical properties of the rocks. These abrupt changes are most likely caused by attenuation and delays of the seismic energy as it passes through the open fracture zones B and C and adjacent altered rock (Figures 2 and 3).

The highly variable nature of the seismograms precluded the use of automatic-picking algorithms. From the total 99,031 seismograms, we were able to pick manually 52,600 first-arrival times (Table 1) with an accuracy of 1–4 ms.

TRAVELTIME TOMOGRAPHY

Tomographic inversion of traveltimes is now a relatively standard procedure (Nolet, 1987). It requires an initial input model, a forward solver to predict traveltimes and raypaths, an appropriate regularization scheme, and a solver for the inversion problem. Finally, the quality of the tomograms must be estimated.

Initial model

Our input model had a velocity of 1200 m/s at the surface and a constant linear gradient of 15 s^{-1}. Above the surface, the velocity was fixed to 300 m/s. Several tests (e.g., Lanz et al., 1998) demonstrated that the input velocity and velocity gradient were not critical; a variety of different input models produced comparable results.

Forward problem

Solution of the 2D forward problem was achieved using the procedure described by Lanz et al. (1998). The algorithm proposed by Podvin and Lecomte (1991) was employed for the 3D traveltime computations, and the steepest descent method of Aldridge and Oldenburg (1993) was used to construct the 3D raypaths. For both the 2D and 3D forward solvers, the lengths of cell boundaries were uniformly 1.5 m.

Regularization

Following Lanz et al. (1998), we accounted for underdetermined components of the inversion problem by using damping and smoothing constraints. The following system of equations had to be solved:

$$\begin{pmatrix} \mathbf{t} \\ \mathbf{h} \end{pmatrix} = \begin{pmatrix} \mathbf{L} \\ \mathbf{D} \end{pmatrix} \mathbf{s}, \tag{2}$$

where $\mathbf{t}$ contains the observed traveltimes, $\mathbf{L}$ is the Jacobian matrix that includes the traveltime derivatives, $\mathbf{h}$ and $\mathbf{D}$ are the regularization constraints, and $\mathbf{s}$ contains the slowness estimates. The traveltime derivatives in $\mathbf{L}$ are equal to the ray segments L_{ijk} ($t_{ij} = L_{ijk} s_k$), where the i and j indices represent the sources and receivers and the k indices are the elements of the slowness vector $\mathbf{s}$. Relatively low lev-

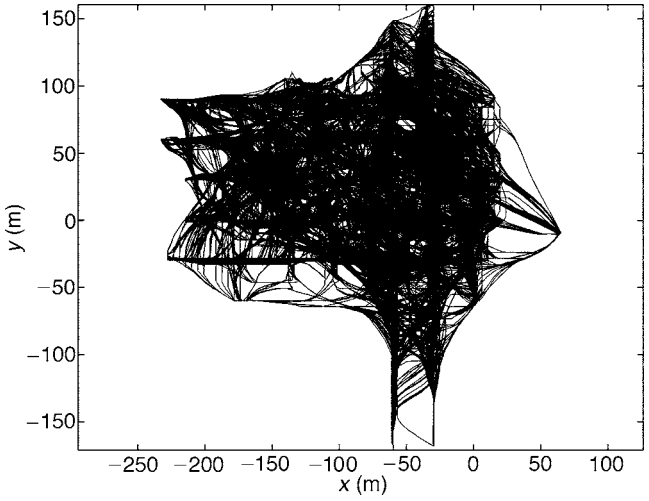

Figure 4. Top view of the raypath distribution for the final 3D tomogram (after 10 iterations).

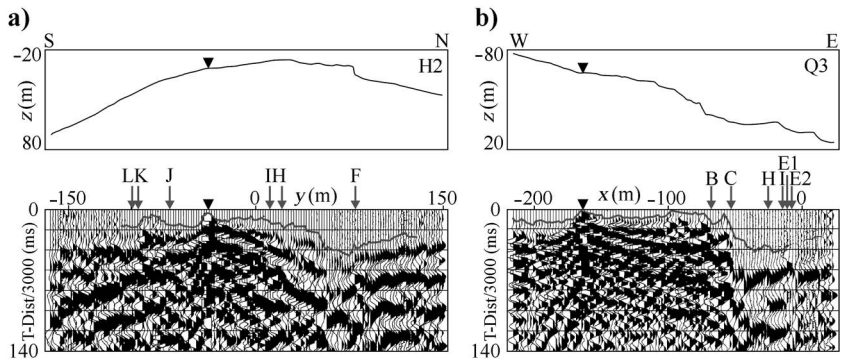

Figure 5. Examples of shot gathers from profiles (a) H2 and (b) Q3 (for locations of the relevant shots see purple crosses in Figure 3). Both gathers are plotted with a 3000 m/s reduction velocity. Black triangles indicate the shot locations, lines show the first-arrival picks, and arrows with letters mark the positions of surface fractures. Elevations of receivers relative to the top of borehole SB120 are displayed above the seismic records. Additional shot gathers are shown in Figure B-1 of Appendix B.

els of damping and smoothing produced stable results for all 2D and 3D tomographic inversions. The inversion schemes were controlled 5% by the damping, 20% by the smoothing, and 75% by the data.

Inverse problem

The matrix of the right-hand side of equation 2 is extremely sparse, so the system of equations can be suitably solved with the LSQR algorithm proposed by Paige and Saunders (1982). For the 2D and 3D tomographic inversions, cell sizes of 3×3 m and $4.5 \times 4.5 \times 4.5$ m, respectively, proved to be suitable.

Quality appraisal

It is important to be able to distinguish between well-resolved and poorly resolved features in the tomograms. We illustrate our approach for estimating the reliability of an inversion by analyzing the 2D tomogram derived from profile Q4 data (Figure 6a). Figure 6b demonstrates that only the upper 12–50 m of ground beneath the undulating surface is sampled by rays of the final Q4 tomogram. Clearly, velocities in regions of the tomogram not sampled by rays in the final model are not resolved by the first-arrival traveltime data. It is noteworthy that the maximum depth of resolved velocities varies markedly along the length of the profile.

Ray coverage provides only partial information about the spatial resolution. Some rays near the bottom of the sampled region in Figure 6b are subparallel, suggesting that the raypaths are controlled by a strong velocity gradient roughly perpendicular to the surface topography. Although such a ray pattern provides good resolution perpendicular to the raypaths, it suffers from poor resolution parallel to them. A measure of resolution that accounts for the angular coverage of the rays is required. We employ the ray density tensor (Kissling, 1988) for this purpose. For each cell, the ray segments are inserted into an $n \times 2$ (for 2D tomography) or $n \times 3$ (for 3D tomography) matrix $\mathbf{M}$, where n is the number of ray segments within a particular cell and the columns contain the components of the individual segments. The eigenvectors and eigenvalues of the matrix $\mathbf{M}^T\mathbf{M}$ describe the principal axes of an ellipse (2D) or ellipsoid (3D) that reflect the angular distribution of the ray segments. The ratios of smallest to largest eigenvalues are then measures of resolution, whereby ratios of one indicate uniform angular distributions and ratios of zero are diagnostic of parallel rays. Figure 6c shows the distribution of eigenvalue ratios for profile Q4. It demonstrates that velocities are generally well resolved in those parts of the tomogram sampled by rays. Exceptions are the lower regions where the raypaths are mostly subparallel to each other.

To emphasize the well-resolved regions of the tomogram, we use a semitransparent mask to cover those parts of the tomogram not sampled by rays, and to highlight the most significant variations in velocity we limit the color scale to 500–3800 m/s (velocities $<$ 500 m/s are blue and velocities $>$3800 m/s are reddish-brown). The final representation of the Q4 tomogram is displayed in Figure 6d. It reveals a clear lateral transition from relatively high to low velocities near $x = -75$ m. According to the ray coverage in Figure 6b, the base of the lowest velocity region is relatively well constrained, but the eigenvalue ratios in Figure 6c indicate that lateral resolution within the basal part of the low-velocity region is poor.

RESULTS FROM THE 2D TOMOGRAPHIC INVERSIONS

The final 2D tomograms and depth projections of fracture zones and faults A–L (see Figure 2) based on surface geological mapping, surface and borehole georadar observations and borehole logs are displayed in Figure 7. Profile H1, which trends perpendicular to the dominant slope direction, is quite short (126 m), such that the depth penetration of rays to the surface receivers does not exceed 25 m. The highly variable velocity structure beneath this profile is not surprising because it is located close to the rockfall scarp (Figures 2 and 3). Profiles H2 and H3 are much longer (324 and 315 m), thus providing velocity information to depths $>$50 m in their central regions. In the tomograms of both profiles, large zones distinguished by remarkably low velocities (i.e., ultralow velocities $<$1500 m/s and very low velocities of 1500–2700 m/s) are juxtaposed against blocks of rock with higher velocities. It is noteworthy that most of the extrapolated fracture zones and fault traces lie within regions that have ultralow velocities.

Similar zones of very low velocity adjacent to higher velocity blocks are seen in the tomograms for the slope-parallel profiles Q1-Q5 (Figure 7), all of which are 238 m long (Table 1). The lateral extent of the ultralow-velocity zones decreases uniformly from profile Q1 ($\sim$130 m) to Q5 ($\sim$50 m). Again, most of the fracture zones and faults occur within the ultralow-velocity zones.

Our 2D tomograms delineate a significant volume of very-low-velocity crystalline rock. To image better the areal extent of very-low-velocity material, Figure 8a shows a plan view of velocity val-

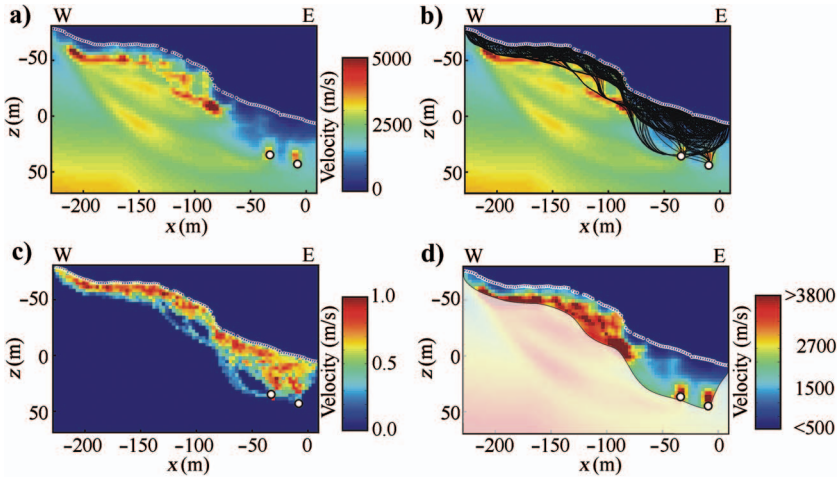

Figure 6. (a) A 2D tomogram for profile Q4. Surface and borehole receiver positions are identified by small white circles and blue dots, respectively. (b) As for (a), but with ray coverage for the final 2D tomogram. (c) Ratios of smallest to largest eigenvalues of the ray density tensors. (d) As for (a), but with the color scale limited to 500–3800 m/s (values $<$500 m/s are blue and those $>$3800 m/s are reddish-brown) and regions characterized by poor resolution covered by a semitransparent mask. The z-coordinates are relative to the top of borehole SB120. For shot locations, see Figure 3.

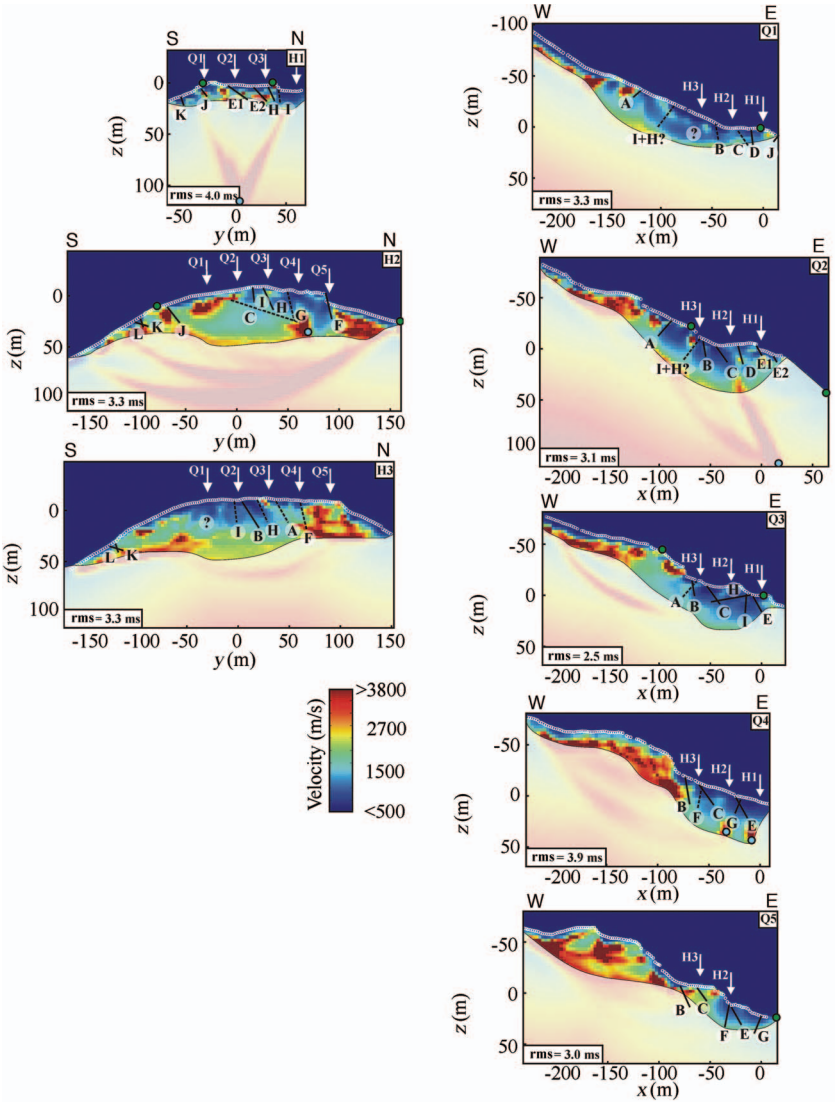

Figure 7. 2D tomograms for all profiles (see also Figure 3). Most details are explained in the caption to Figure 6. White arrows show the intersection points of crossing profiles. Solid black lines delineate the locations of fracture zones based on surface geological mapping, surface and borehole georadar observations and borehole logs, whereas dashed black lines are the extrapolated projections of nearby fracture zones into the cross sections. rms is the root-mean-square difference between the tomographic-model predicted and observed traveltimes.

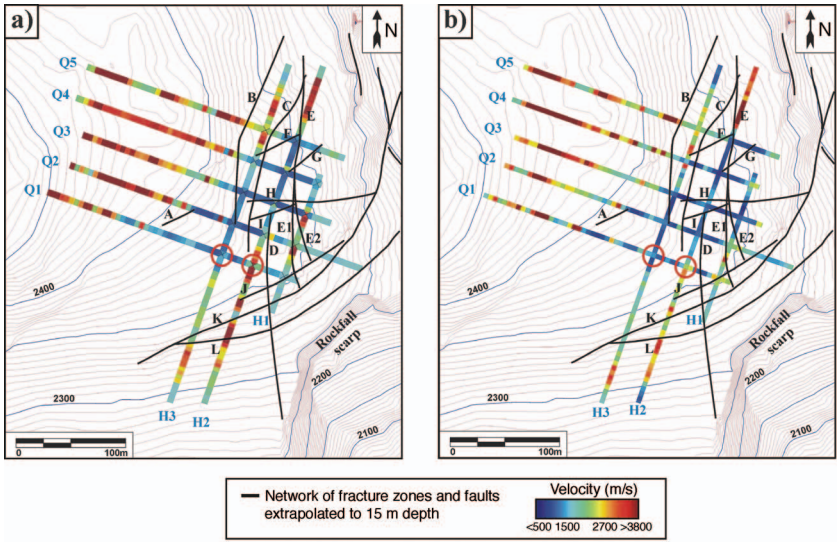

Figure 8. (a) P-wave velocities extracted from the 2D tomograms (Figure 7) at 15 m depth and depth-extrapolated positions of fracture zones and faults A-L (Figure 2). The velocity-depth relationships and traveltime curves in Figure 9 are associated with the regions marked by the red circles. (b) P-wave velocities at 15 m depth extracted from the 3D tomogram along all profiles. All other details are as for (a).

ues observed in the 2D tomograms at 15 m depth below the surface. Evidently, ultralow to very low velocities extend over much of the eastern volume of rock sampled by our seismic profiles.

Inconsistencies between the 2D tomograms

In areas characterized by very high lateral velocity contrasts and anisotropy, it is appropriate to question the use of 2D isotropic tomographic approaches; first arriving energy may travel along raypaths that deviate substantially from the planes containing the profiles. One means of assessing the significance of these issues is to compare velocity-depth functions extracted from crossing profiles at their intersection points. Close inspection of Figure 8a and b demonstrates that only eight of the 14 pairs of coincident velocity values at 15 m depth are the same to within ~20%. We explore this further by analyzing the two pairs of coincident velocity-depth functions shown in Figure 9a–d. Velocity-depth functions obtained from profiles H2 and Q1 at their intersection point differ markedly (Figure 9a), whereas those of profiles H3 and Q1 oscillate about a common trend (Figure 9c). These differences and similarities are consequences of the differences and similarities of the first-arrival traveltime curves recorded along the pairs of intersecting profiles. A shot detonated at the intersection of profiles H2 and Q1 generates quite different traveltime curves along the respective profiles (Figure 9a), whereas a shot detonated at the intersection of profiles H3 and Q1 generates very similar traveltime curves in the two directions (Figure 9d).

There are at least three explanations for the velocity mismatches at some profile intersections: (1) mineral anisotropy related to the foliation of the crystalline rocks, (2) macroscopic anisotropy caused by the fracture zones and faults, and (3) strong velocity gradients perpendicular to the profiles (i.e., 3D heterogeneity associated with the fracture zones and faults). The average foliation-related anisotropy revealed by velocity measurements on the core samples is about 13% at 20 MPa, with velocities higher in the foliation plane than perpendicular to it. Consequently, this orientation of anisotropy cannot explain the velocity mismatches. Instead, the distribution of very low velocities in Figure 7 and the mismatches of velocities at the crossover points in Figure 8 suggest that macroscopic anisotropy and 3D heterogeneity associated with fracture zones and faults are the dominant effects. We have neither sufficient data nor an appropriate computer code to account for the effects of macroscopic anisotropy beneath our investigation site. In the following, we attempt to estimate the influence of 3D velocity heterogeneity, but acknowledge that macroscopic anisotropy may influence the results somewhat.

RESULTS FROM THE 3D TOMOGRAPHIC INVERSIONS

To estimate the resolving power of our 3D experimental procedure, we conducted two sensitivity tests. The results of these tests (Appendix A) demonstrated that our source-receiver configuration was suitable for delineating broad-scale structures from the surface to depths of 30–50 m.

Comparison of the 2D and 3D inversion results

To compare the results of the 2D and 3D approaches as applied to the Randa first-arrival data, we have extracted from the 3D tomogram the following information:

- Velocity-depth functions at selected intersections of the 2D profiles (Figure 9a and c)
- Cross sections that coincide with all 2D profiles (Figure 10)
- Velocity values within these cross sections at 15 m depth below the surface (Figure 8b)

The velocity-depth functions based on the final 3D tomogram lie between those derived from the corresponding 2D tomograms in Figure 9a and c, and the traveltimes predicted by the 3D tomogram

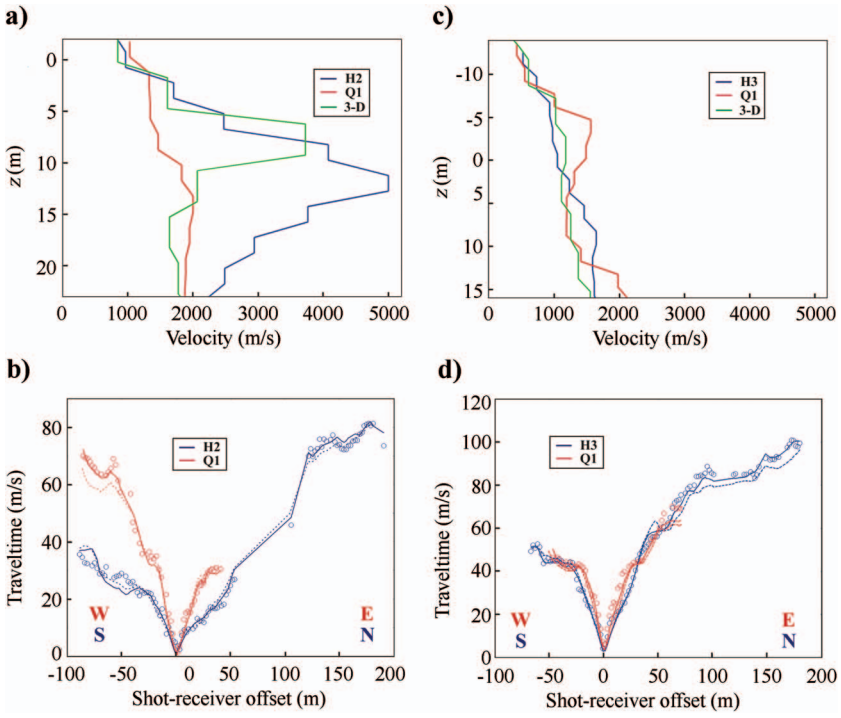

Figure 9. Velocity-depth functions extracted from the 2D and 3D tomograms at the intersections of profile Q1 with profiles (a) H2 and (c) H3 (for locations see Figure 8). (b) and (d) Observed (circles) and predicted (red lines = profile Q1; blue lines = profiles H2 and H3) traveltimes for shots generated at the intersections of profile Q1 with profiles H2 and H3, and receivers deployed along the respective profiles. Solid lines are based on the 2D tomograms, whereas the dashed lines are based on the 3D tomogram.

match the observations almost as well as those predicted by the 2D tomograms (Figure 9b and d). The relatively large mismatches of some traveltimes predicted by the 3D tomograms at longer offsets (e.g., at distances >50 m for Q1 in Figure 9b and at distances >100 m for H3 in Figure 9d) are not general features of the 3D results. As indicated in Figure 7, the root mean square (rms) differences between traveltimes based on the 2D tomograms and the observations range from 2.5 to 4.0 ms. For the 3D tomogram, the rms difference is 5.2 ms, which is only slightly above the estimated picking accuracy. Considering that the 3D model should be a more realistic approximation to the true subsurface structure than the 2D tomograms, one might have anticipated a lower rms difference. We suspect that the slightly higher than expected rms difference is from the effects of macroscopic anisotropy and the relatively large cell size ($4.5\times4.5\times4.5$ m) employed for the 3D inversions.

The general patterns of low and high velocity values in the cross sections of Figure 10 are similar to those in the 2D tomograms of Figure 7, but the overall depth penetration is somewhat larger in the former. It is noteworthy that the estimated trends of several fracture zones and faults coincide more closely with velocity minima in the extracted cross sections than in the 2D tomograms (e.g., E2 beneath profile H1, F beneath profile H3, D beneath profile Q2, and A beneath profile Q3).

Inconsistencies of velocities at the intersection points of crossing profiles in Figure 8a are not seen in Figure 8b. Nevertheless, the general distributions of high and low velocities at 15 m depth are alike in the 2D and 3D tomograms. Figure 8a and b shows a broad zone of crystalline rock with ultralow to very low velocities juxtaposed against blocks of rock with higher, but still quite low velocities.

Velocity distribution based on the 3D tomogram

Areal distributions of velocities at 5-m depth intervals below the surface are presented in Figure 11. Only those cells sampled by at least three rays are displayed. The corresponding eigenvalue ratios in Figure 12 suggest that the velocities are relatively well resolved to ~30 m depth. Below this level, the rays in each cell are roughly parallel to each other, such that only the broad-scale features are likely to be meaningful.

Ultralow velocities can be traced through the entire depth range of the well-resolved regions of the tomogram (Figures 10 and 11). Furthermore, despite the rather limited ray coverage below 30 m depth, there is clear evidence for ultralow velocities extending to depths as great as 40 m and very low velocities continuing at some locations to the base of the surveyed volume near 50 m depth. The depth slices indicate a high degree of heterogeneity throughout the investigated rock mass. Within the broad zone of ultralow to very low velocities, there are blocks of higher velocity material and within the volume of generally higher velocities there are bands of ultralow to very-low-velocity rock.

Reliability of the anomalously low velocities

Considering the abrupt lateral changes seen in many Randa shot gathers (e.g., Figure 5), it is feasible that the nature of the seismic energy changes as it crosses some major fracture zones and faults. For example, direct and refracted P-waves absorbed at large open fracture zones may be replaced at longer distances and at later times by P-waves generated as a result of Rayleigh- to-P-wave conversions at the same discontinuities. These effects are not taken into account in first-arrival traveltime tomography. On the other hand, we see first arrivals propagating with ultralow to very low apparent velocities directly from all shots detonated across a broad zone of the mountain slope (Figure 8). Since first arrivals with anomalously low apparent velocities (i.e., <2700 m/s) are observed uninterrupted from the shotpoints to distances in excess of 100 m (e.g., Appendix B), there

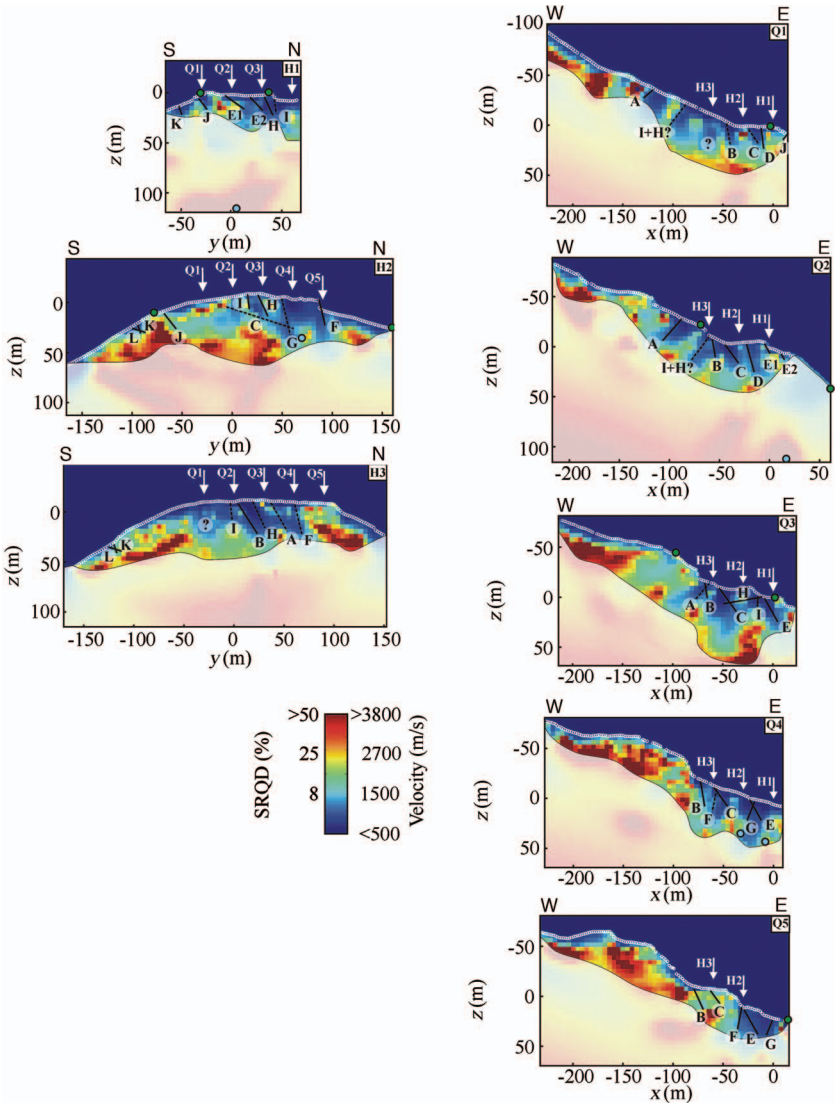

Figure 10. Vertical cross sections through the 3D tomographic model along the 2D profiles. Explanations for most details are given in the captions to Figures 6 and 7.

is little doubt that such velocities extend to considerable depths. Moreover, independent support for the existence of anomalously low velocities to a depth of at least 30 m is provided by stacking velocity analyses of reflections recorded on profile H2 data. A velocity of 850 ± 100 m/s is required to stack a 60-m-long band of reflections at traveltimes of 40–70 ms.

It is not possible to account quantitatively for the influence of macroscopic anisotropy and the effects of strong P-wave absorption and mode conversions at the major fracture zones and faults. Nevertheless, the general distribution of anomalously low velocities portrayed in Figures 10 and 11 is likely to be a reasonable first-order approximation to the actual situation in the subsurface.

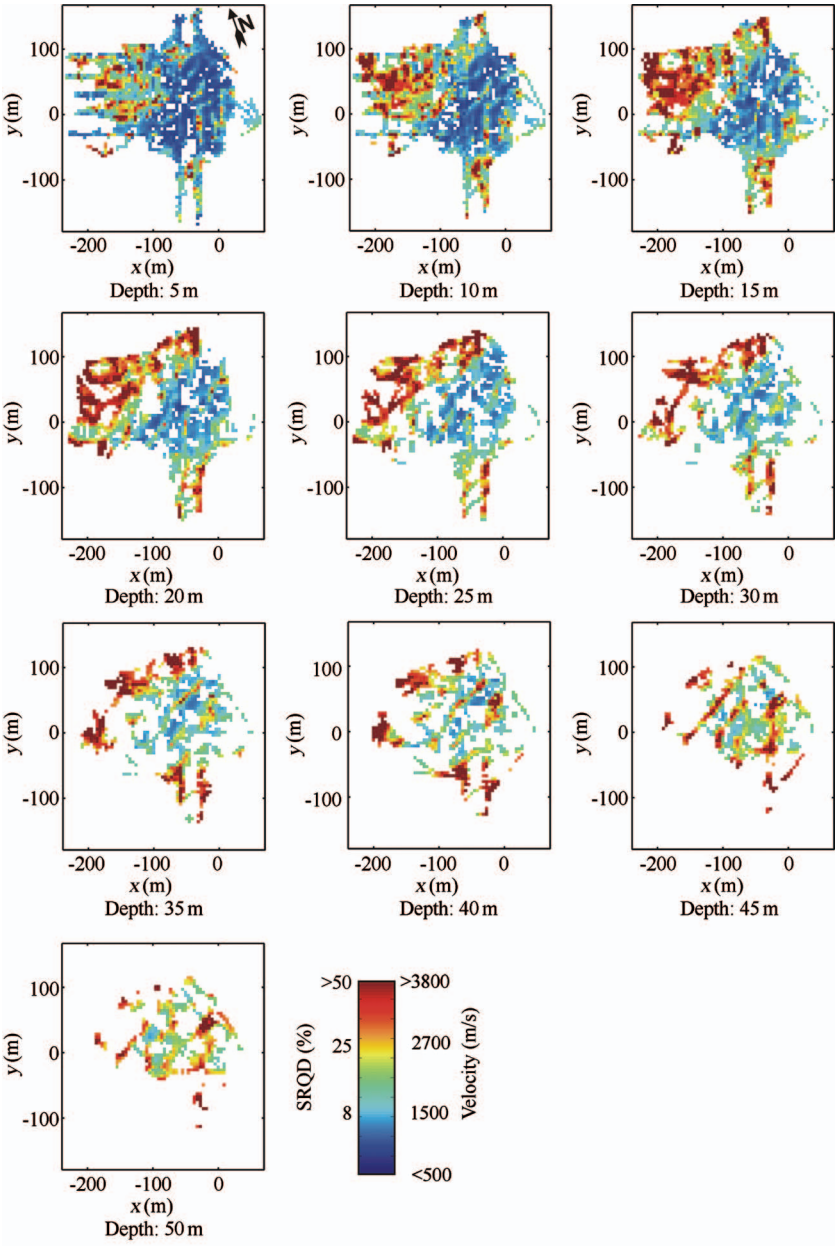

Figure 11. Various depth slices (parallel to topography) through the 3D tomographic model. Only those cells hit by at least three rays are displayed.

INTERPRETATION

To aid the interpretation of the tomograms, Figure 13a shows the depth-extrapolated locations of surface fracture zones and faults plotted on a map of velocities at 15 m depth, and Figure 13b and c shows these features superimposed on maps portraying the thicknesses of cover material and rock with velocities <1500 and <2700 m/s, respectively. At locations where the depth penetration of seismic energy is limited (Figure 10), the thicknesses shown in Figure 13b and c are minimum estimates. The extent of mobile rock determined from geodetic measurements is also outlined in Figure 13a–c.

Figure 13a and b shows ultralow velocities extending through a large volume beneath the investigation site, with velocities <1500 m/s being observed to depths of at least 25 m. Very low velocities of 1500–2700 m/s are observed extending to various depths across the entire surveyed area (Figure 13c).

Source of the anomalously low velocities

Numerous theoretical studies and laboratory and field investigations demonstrate that cracks, fractures, and faults have a major influence on the elastic properties of crystalline rock (Walsh, 1965; O'Connell and Budiansky, 1974; Simmons et al., 1975). The presence of water also plays an important role, with the lowest velocities being measured on dry crystalline rock samples (Nur and Simmons, 1969).

Although highly weathered crystalline rock may be characterized by ultralow to very low velocities at shallow depths (see compilation in Hack, 2000), to our knowledge, deep penetrating zones of such anomalously low-velocity crystalline rock have only ever been recorded across unstable or potentially unstable mountain slopes. On the granitic hillslope above the Ananevo rockslide in Kyrgyzstan, velocities of 900 m/s were determined to extend to 35 m depth (Havenith et al., 2002), and similarly low velocities have been traced to a comparable depth beneath a potentially unstable mountain overlooking a Norwegian fjord (L. H. Blikra, 2005, personal communication). We suggest that ubiquitous dry cracks, fracture zones, and open faults at a variety of scales are the most plausible explanation for the anomalously low velocities observed in the Randa data and tomograms. This interpretation is supported by the fact that the major fracture zones and faults are concentrated within regions of ultralow to very low velocity (Figures 10 and 13).

To obtain a very approximate estimate of crack porosity at the Randa investigation site, we follow Mavko et al. (1998) in assuming that the Reuss lower bound provides the most appropriate formula for averaging elastic moduli of rock fragments and air-filled voids. If our interpretation is correct, then $\sim$17% of the Randa subsurface characterized by velocities of $\sim$1500 m/s must be air-filled cracks, fracture zones, and open

faults. This value is close to the upper bound of porosities that Schindler et al. (1993) estimated for the detached rock mass at Randa before it collapsed in 1991. They obtained a 7%–15% range of porosities based on estimates of the (1) volume of material removed from the mountain slope, (2) volume of material contained in the debris fan, (3) porosity of the debris fan, and (4) other more minor factors (e.g., volume of dust spread over adjacent regions and probable depression of land below the debris fan).

Fractures and SRQD values at Randa

Unfortunately, none of the cores from the shallow boreholes at the Randa investigation site were analyzed in terms of the RQD classification system of Deere et al. (1967) before being broken up for other studies, and drilling of the three moderately deep boreholes did not produce cores. Some information on the degree of fracturing with depth is available from televiewer logs, which reveal numerous fractures intersecting the boreholes along their entire lengths (Willenberg, 2004; Spillmann et al., 2006). For example, of the 107-m length of borehole SB120 logged with the televiewer, only seven sections of about 1-m length are fracture free. Other 1-m-long sections have an average of 2.5 fractures per meter. A number of these fracture zones are slowly opening. Comparable results are obtained from the other two boreholes.

To relate the anomalously low P-wave velocities to rock quality, we have marked SRQD values on the color bars of Figures 10, 11, and 13. If it is appropriate to use equation 1 for these very low velocities, then our data suggest that extensive volumes of rock underlying the investigation site have SRQD values $<25\%$.

Although the relationship between P-wave velocity and rock quality is not well defined and the value assumed for the velocity of intact rock may be in error by up to 10%, the ultralow to very low velocities observed at Randa are strong evidence for a large volume of low quality rock.

Distribution of velocities

Not only is the mobile rock mass characterized by ultralow velocities (<1500 m/s), but so too is a large region to the west. Ultralow velocities continue to depths of 25 m and greater in a broad northeast-southwest trending zone (Figure 13b). By taking into account the distribution of very low velocities (1500–2700 m/s), we see that very poor-quality rock underlies most of the investigation site to >35 m depth in the east and 5–10 m depth in the west and south. Moderately large blocks of rock with velocities >3800 m/s are only found in the northwest region of the site (Figure 11). Even in this region, isolated bands of lower velocity material interrupt the continuity of the higher velocity blocks.

Information on the distribution of seismic velocities is limited to the upper 50 m of the mountain slope. The cross sections displayed in Figure 10 suggest that very low to low velocities (<3800 m/s) may continue to greater depths. This possibility is consistent with the numerous fractures identified throughout the length of borehole SB120 (Willenberg, 2004; Spillmann et al., 2006).

Velocity lineaments, surface fracture zones, and the rockfall scarp

The broad zone of ultralow and very low velocities parallels the northeast-southwest trending edge of the rockfall scarp (Figures 11

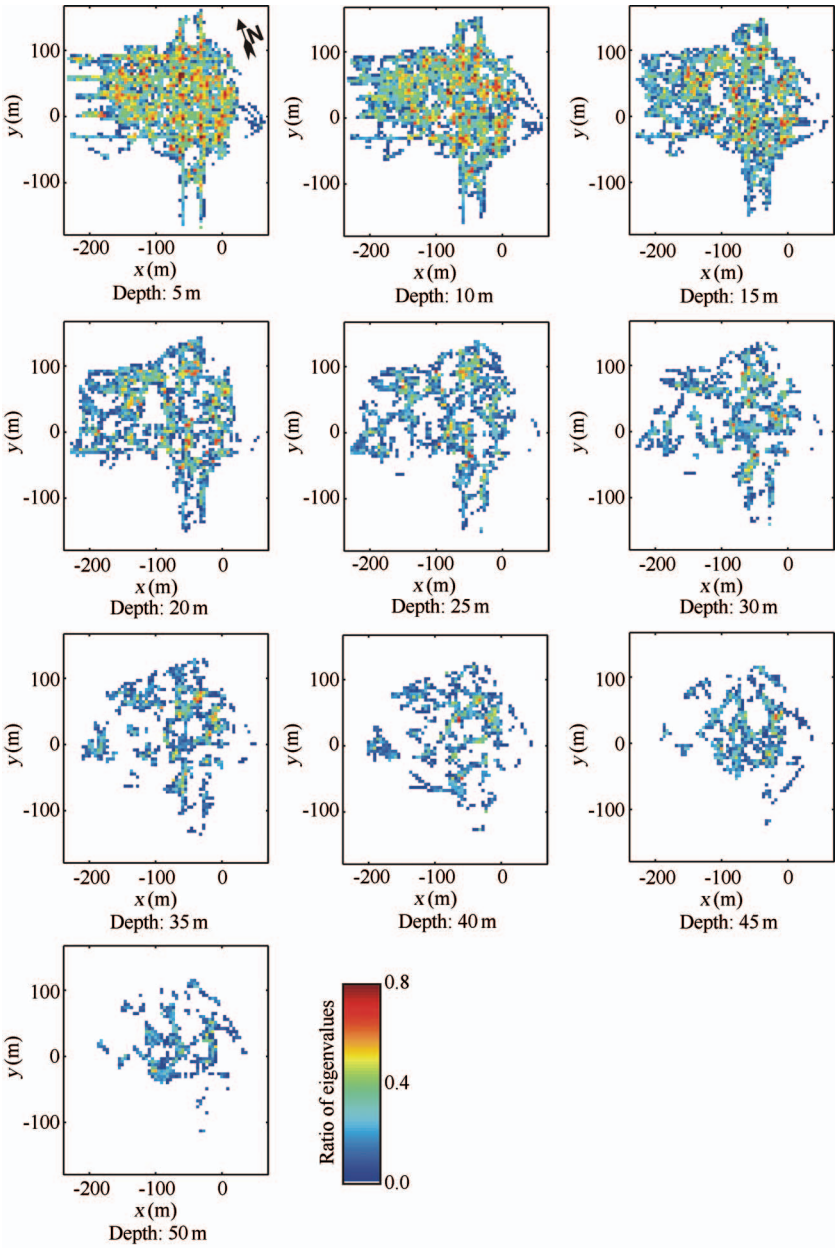

Figure 12. Ratios of smallest to largest eigenvalues corresponding to the depth slices shown in Figure 11.

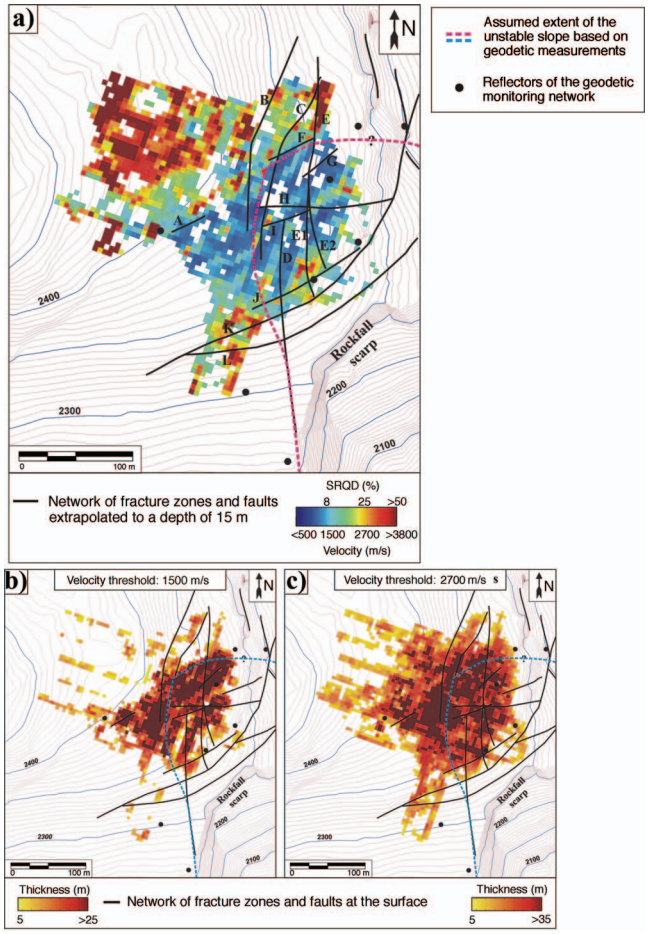

Figure 13. (a) Velocities extracted from the 3D tomogram at 15 m depth below the surface. (b) Thicknesses of near-surface volumes with velocities <1500 m/s (SRQD $<8\%$). (c) Thicknesses of near-surface volumes with velocities <2700 m/s (SRQD $<25\%$). In regions where the depth penetration of seismic energy is limited, the thicknesses shown in (b) and (c) are minimum estimates. The unstable part of the rock mass based on geodetic measurements (Willenberg, 2004) is outlined by the dashed red line in (a) and the dashed blue lines in (b) and (c). Contours are meters above sea level.

and 13a). In addition, some bands of relatively lower velocity in the upper 25 m of our 3D tomogram appear to delineate scarp-parallel fracture zones. Two of these project to surface fracture zones G and I. One prominent low-velocity lineament coincides with and appears to connect surface fractures A and F, yet there is no surface evidence for a link. It is noteworthy that major surface fracture zones J, K, and L, which are not well sampled by the 3D seismic survey, are also subparallel to the northeast-southwest trending part of the rockfall scarp.

CONCLUSIONS

We have recorded a dense seismic data set across a large area that includes an unstable mountain slope overlooking the busy Matter Valley in the Swiss Alps. Inversions of first-arrival traveltimes picked from these data revealed a broad zone of remarkably low seismic velocities that extends well beyond the limits of rock that is known to be currently moving towards the valley. Although the broad-scale lateral and depth distributions of ultralow to very low velocity gneissic rock were well defined in the 2D and 3D tomograms, consistent velocities at the intersections of crossing profiles and several potentially important lineaments were unique to the 3D tomogram.

Ultralow velocities <1500 m/s were mapped throughout a volume that extended over a 200×100-m area and a depth of ~25 m (Figures 10, 11, and 13). Such low velocities in gneissic rock were extraordinary. To explain such low velocities required $\sim17\%$ of the investigated volume to be air-filled voids. Many surface fracture zones and faults transected the broad ultralow-velocity region, the trend of which paralleled part of the scarp generated by the pair of 1991 rockfalls. Very low velocities (1500–2700 m/s) increased the area and thickness of highly anomalous rock to 200×150 m and >35 m, respectively. Ubiquitous dry cracks, fracture zones, and faults were the likely causes of the anomalously low velocities.

Only in the northwest region of the investigation site did we see evidence for moderately large blocks of rock with velocities >3800 m/s. Several small bands of lower-velocity material appeared within these higher-velocity blocks.

Assuming that movements identified by the geodetic measurements continue in the future, the mobile rock mass will eventually fall into the valley below. The collapse may occur gradually or as one or more discrete large falls. As this mass becomes completely detached from the mountain, support for the adjacent highly fractured rock will decrease substantially on its southeastern flank, probably resulting in another phase of mountain slope instability. A two-stage sequence of rockfalls, much like that of the 1991 events, is then possible. Based on the widespread distribution of anomalously low velocities, we suggest that estimates of the volume of crystalline mass susceptible to catastrophic collapse need to be reassessed and that future monitoring of the mountain slope should account for the entire area underlain by rock characterized by ultralow to very low seismic velocities. In particular, additional geodetic reflectors should be established west and southwest of the line delineating the boundary between mobile and stationary rock, and 3D kinematic numerical models that account for the topography, geology, geotechnical information, and extensive volume of anomalously low velocity need to be developed.

ACKNOWLEDGMENTS

We thank Baptiste Dafflon for performing the borehole core measurements; Giovanni Piffaretti, Ueli Meier, and Simon Lloyd for writing some of the MATLAB scripts and picking the first-arrival traveltimes; Keith Evans, Erik Eberhardt, and Simon Löw for their collaboration in this interdisciplinary project; and J. D. Rouiller and colleagues at the Centre de Recherche sur l'Environment ALPin (CREALP) for their logistical support. Numerous ETH students participated enthusiastically in the field campaign. We appreciate the advice and suggestions provided by Alastair McClymont, Heinrich Horstmeyer, Rita Streich, Jens Tronicke, the journal reviewers, and the journal editors. The research was funded by the Swiss National Science Foundation.

APPENDIX A

SENSITIVITY TESTS

We have conducted two sensitivity tests to determine the ability of our seismic data to delineate the regions of ultralow to very-low-ve-

locity. For the first test, we inserted two wedge-shaped anomalies of 500 m/s into the initial 3D velocity model employed for our tomographic inversions. Both anomalies were 75 m long, 30 m wide, and 70 m deep. They were separated by a 15-m gap and oriented slightly oblique to the H-profiles (Figures 3 and A-1a). Synthetic traveltimes were computed using all shot-receiver combinations from the observed data set. Because we were interested in the theoretical resolution power of our layout, no noise was added to the synthetic data.

Slices parallel to the topography through the 3D tomogram are shown in Figure A-1. The northern anomaly is imaged faithfully down to a depth of 45 m, although its shape is somewhat distorted below 15 m. The southern anomaly that extends beyond the crossing area of the H and Q profiles is less well resolved. Beyond 30 m depth, it is difficult to recognize its signature in the horizontal slices.

Vertical sections extracted at $y = 50$ m and $y = -50$ m are shown in Figure A-2. The large number of crossing rays allows the northern anomaly along $y = 50$ m to be imaged reliably down to a depth of about 50 m. The profile at $y = -50$ m lies outside of the crossing area of the H and Q profiles. Spatial resolution is, therefore, markedly reduced. Nevertheless, the southern anomaly can be traced down to a depth of about 30 m.

Our second sensitivity test first involved computing first-arrival traveltimes for a smoothed version of our final 3D velocity tomogram using the same source-receiver configurations shown in Figures 2 and 3. After adding random errors with a variance of 2 ms (the reading accuracy of our original data varied from 1 to 4 ms), the synthetic traveltimes were inverted using the same procedures employed for the field data. Although there were differences in detail between our final 3D velocity model and the 3D velocity model based on the synthetic traveltimes, all important features were common to the two models (Figure A-3).

From our synthetic experiments, we conclude that in the crossing area of the H and Q profiles, low-velocity features can be imaged down to a maximum depth of 30–50 m. Outside of this area, it is still possible to estimate the lateral extent of low-velocity features, but depth resolution is restricted to 20–30 m.

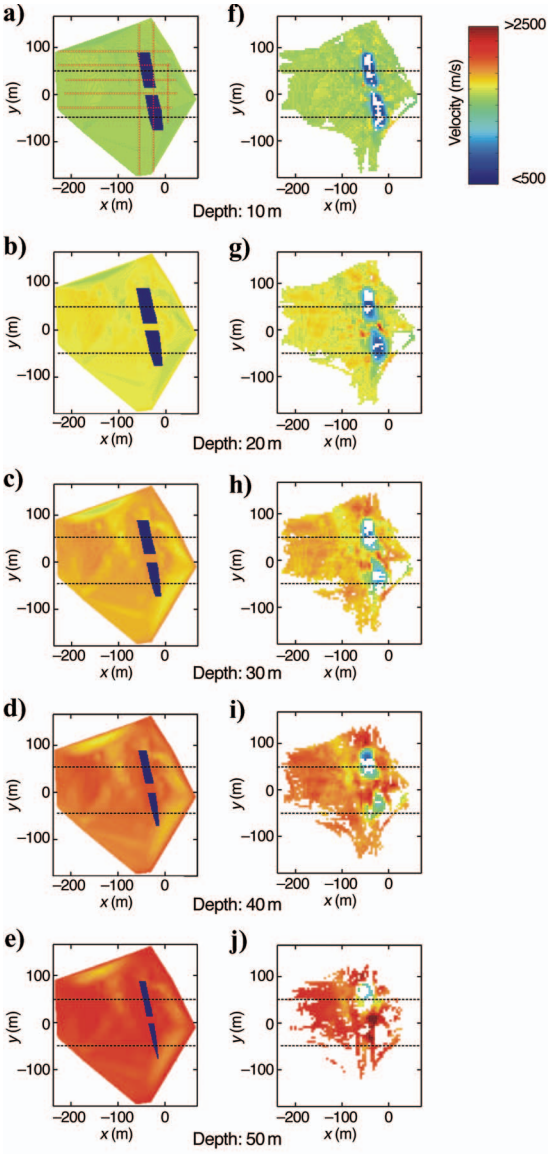

Figure A-1. (a)–(e): Depth slices parallel to the topography through a synthetic velocity model; (a) also shows the locations of simulated profiles H1 to H3 and Q1 to Q5 (see also Figure 3). The positions of the vertical sections shown in Figure A-2 are displayed as dashed black lines. (f)–(j) Results of 3D tomographically inverting synthetic data based on the model shown in the corresponding (a) to (e) panels and the source-receiver configurations of the observed data set (i.e., Figure 3).

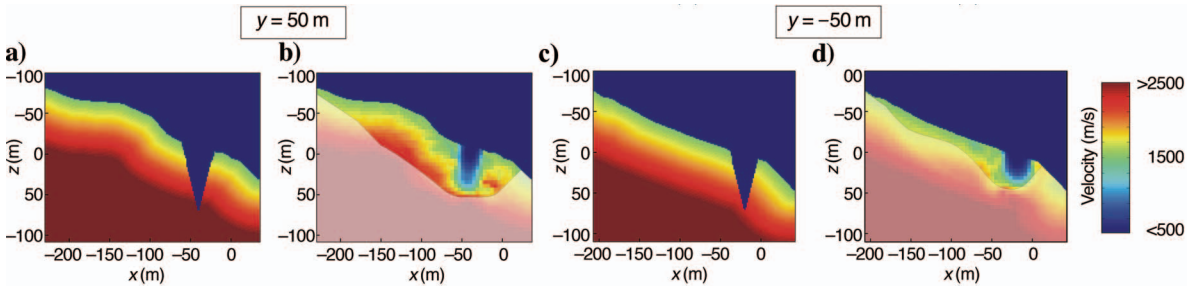

Figure A-2. Vertical sections along the dashed black lines shown in Figure A-1. (a) and (c) True model. (b) and (d) Tomographic reconstructions with regions characterized by poor resolution covered by a semitransparent mask.

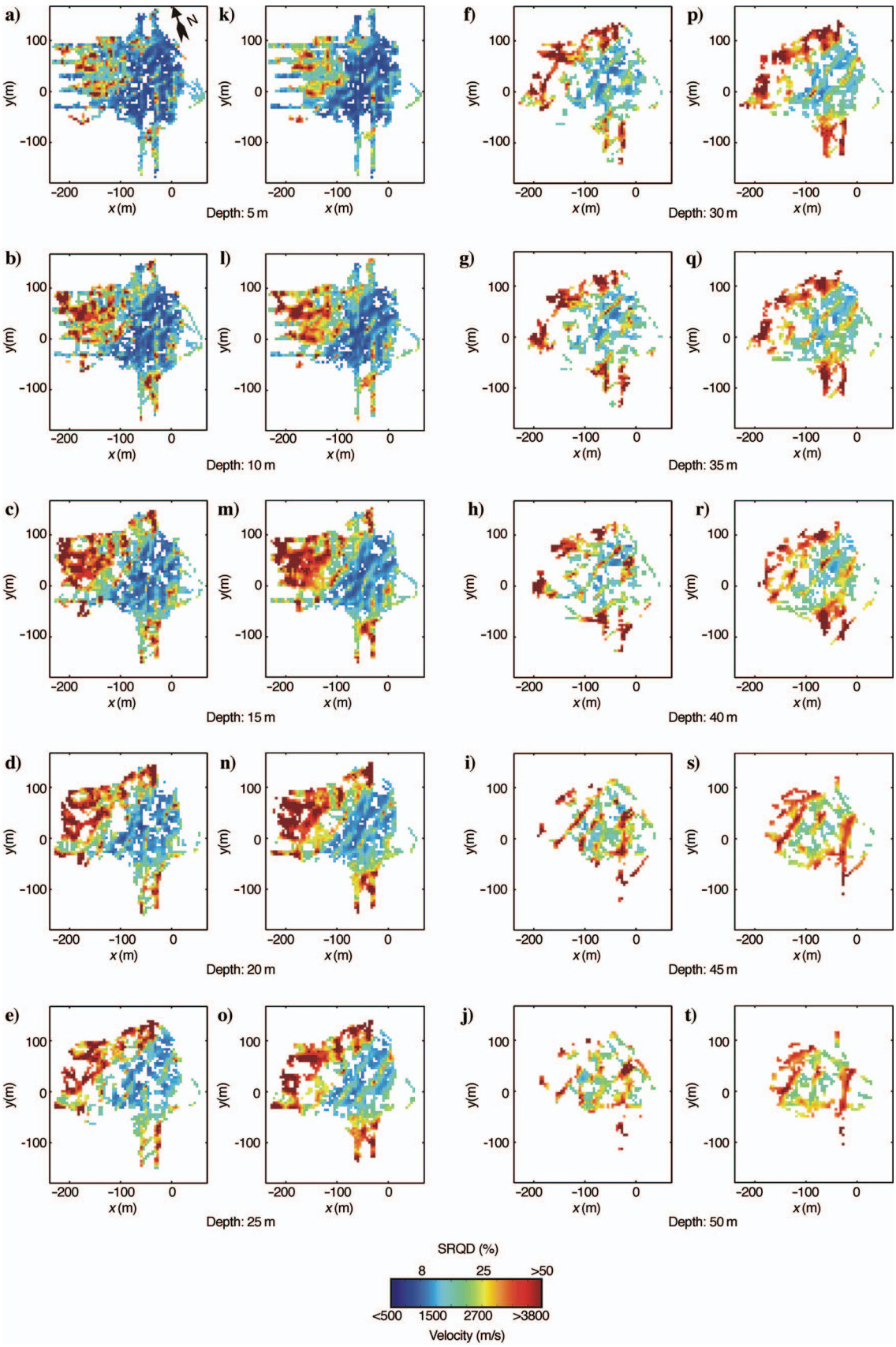

Figure A-3. Comparison of the depth slices shown in Figure 11 (a)–(j) with the results of the second sensitivity test (k)–(t) described in this appendix.

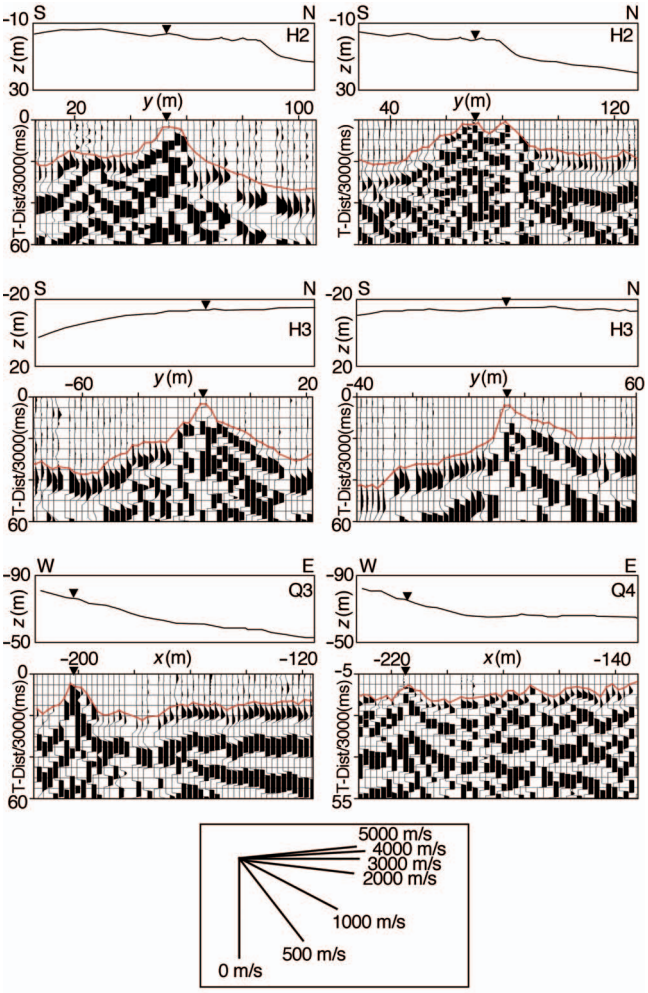

Figure B-1. Portions of typical shot gathers showing the very low apparent velocities of first arrivals recorded along seismic profiles H2 and H3 and the higher apparent velocities of first arrivals recorded along the northeastern ends of profiles Q3 and Q4. All shot gathers are plotted with a 3000-m/s reduction velocity.

APPENDIX B

SHOT GATHERS

To demonstrate the veracity of the ultralow velocities observed in the Randa tomograms, portions of typical shot gathers recorded along seismic profiles H2 and H3 are presented in Figure B-1. For comparison purposes, portions of shot gathers with more normal crystalline rock velocities (from seismic profiles Q3 and Q4) are also displayed.

REFERENCES

Aldridge, D. F., and D. W. Oldenburg, 1993, Two-dimensional inversion with finite-difference traveltimes: Journal of Seismic Exploration, **2**, 257–274.

Bader, S., and P. Kunz, eds., 1998, Klimarisiken — Herausforderung für die Schweiz (Climatic hazards—Challenges for Switzerland): Hochschulverlag.

Birch, A. F., 1960, The velocities of compressional waves in rocks to 10 kilobars (Part 1): Journal of Geophysical Research, **65**, 1083–1102.

Bruno, F., and F. Marillier, 2000, Test of high-resolution seismic reflection and other geophysical techniques on the Boup landslide in the Swiss Alps: Surveys in Geophysics, **21**, 333–348.

Burlini, L., L. Arbaret, G. Zeilinger, and J.-P. Burg, 2005, High-temperature and pressure seismic properties of a lower crustal prograde shear zone from the Kohistan Arc, Pakistan: Geological Society of London, Special Publication, 245, 187–202.

Cooke, R. U., and J. C. Doornkamp, 1990, Geomorphology in environmental management — A new introduction: Oxford Univ. Press.

Crozier, M. J., and T. Glade, 2005, Landslide hazard and risk: Issues, concepts and approaches, *in* T. Glade, M. Anderson, and M. J. Crozier, eds., Landslide hazard and risk: John Wiley & Sons, Inc., 1–40.

Cummings, D., 2000, Transient electromagnetic survey of a landslide and fault, Santa Susanna Mountains, southern California: Environmental and Engineering Geoscience, **6**, 247–254.

Deere, D. U., A. J. Hendron Jr., F. D. Patton, and E. J. Cording, 1967, Design of surface and near-surface construction in rock: Proceedings of the 8th Symposium on Rock Mechanics, 237–302.

Dussauge-Peisser, C., M. Wathelet, D. Jongmans, D. Hantz, B. Couturier, and M. Sintes, 2003, Investigation of a fractured limestone cliff (Chartreuse Massif, France) using seismic tomography and ground-penetrating radar: Near Surface Geophysics, **1**, 161–170.

Eberhardt, E., H. Willenberg, S. Loew, and H. M. Maurer, 2001, Active rockslides in Switzerland — Understanding mechanisms and processes: International Conference on Landslides — Causes, Impacts and Countermeasures, International Association of Engineering Geology, Expanded Abstracts, 25–34.

Erismann, T. H., and G. Abele, 2001, Dynamics of rockslides and rockfalls: Springer-Verlag.

Gebrande, H., H. Kern, and F. Rummel, 1982, Elasticity and inelasticity, *in* G. Angenheister, ed., Physikalische Eigenschaften der Gesteine (Physical properties of rocks): Springer-Verlag, 1–99.

Gerrard, A. J., 1988, Rocks and landforms: Unwin Hyman.

Govi, M., G. Gullà, and P. G. Nicoletti, 2002, Val Pola rock avalanche of July, 28, 1987 in Valtelina (central Italian Alps), *in* S. G. Evans and J. V. DeGraffin, eds., Catastrophic landslides — Effects, occurrence and mechanisms: Geological Society of America, 71–89.

Hack, R., 2000, Geophysics for slope stability: Surveys in Geophysics, **21**, 423–448.

Havenith, H.-B., D. Jongmans, K. Abdrakhmatov, P. Trefois, D. Delvaux, and I. A. Torgoev, 2000, Geophysical investigations of seismically induced surface effects: Case study of a landslide in the Suusamyr Valley, Kyrgyzstan: Surveys in Geophysics, **21**, 349–369.

Havenith, H.-B., D. Jongmans, E. Faccioli, K. Abdrakhmatov, and P.-Y. Bard, 2002, Site effect analysis around the seismically induced Ananevo rockslide, Kyrgyzstan: Bulletin of the Seismological Society of America, **92**, 3190–3209.

Heim, A., 1932, Landslides and human lives (original title, Bergsturz und Menschenleben; N. Skermer, translator, 1989): BiTech Publishers Ltd.

Heincke, B., A. G. Green, J. van der Kruk, and H. Horstmeyer, 2005a, Acquisition and processing strategies for 3D georadar surveying a region characterized by rugged topography: Geophysics, **70**, K53–K61.

Heincke, B., A. G. Green, J. van der Kruk, and H. Willenberg, 2005b, Semblance-based topographic migration (SBTM): A method for identifying fracture zones in 3-D georadar data: Near Surface Geophysics, **4**, 79–88.

Hudson, J. A., 1992, Rock engineering systems: Theory and practice: High Plain Press.

Jaboyedoff, M., P. Ornstein, and J.-D. Roullier, 2004, Design of a geodetic database and associated tools for monitoring rock-slope movements: The example of the top of Randa rockfall scar: Natural Hazards and Earth System Sciences, **4**, 187–196.

Jahns, E., S. Siegesmund, and T. Chlupác, 1994, In situ seismic velocities versus laboratory measurements: An example from the KTB: Scientific Drilling, **4**, 215–226.

Jongmans, D., P. Hemroulle, F. Demanet, F. Renardy, and Y. Vanbrabant, 2000, Application of 2-D electrical and seismic tomography techniques for investigating landslides: European Journal of Environmental and Engineering Geophysics, **5**, 75–89.

Kissling, E., 1988, Geotomography with local earthquake data: Reviews of Geophysics, **26**, 659–698.

Kopf, M., 1977, Fortschritte der Petrophysik (Advances in petrophysics), *in* R. Lauterbach, ed., Physik der Erdkruste (Physics of the earth's crust): Akademie-Verlag.

Lanz, E., H. R. Maurer, and A. G. Green, 1998, Refraction tomography over a buried waste disposal site: Geophysics, **63**, 1414–1433.

Lapenna, V., P. Lorenzo, A. Perrone, S. Piscitelli, E. Rizzo, and F. Sdao, 2005, 2D electrical resistivity imaging of some complex landslides in Lucanian Apennine chain, southern Italy: Geophysics, **70**, B11–B18.

Martí, D., R. Carbonell, A. Tryggvason, J. Escuder, and A. Pérez-Estaún, 2002, Mapping brittle fracture zones in three dimensions: High resolution traveltime seismic tomography in a granitic pluton: Geophysical Journal International, **149**, 95–105.

Mavko, G., T. Mukerji, and J. Dvorkin, 1998, The rock physics handbook: Tools for seismic analysis in porous media: Cambridge Univ. Press.
McCann, D. M., and A. Forster, 1999, Reconnaissance geophysical methods in landslide investigations: Engineering Geology, **29**, 59–87.
Morey, D., and G. T. Schuster, 1999, Palaeoseismicity of the Oquirrh fault, Utah from shallow seismic tomography: Geophysical Journal International, **138**, 25–35.
Müller, L., 1968, New considerations on the Vaiont slide: Felsmechanik und Ingenieurgeologie, **6**, 1–91.
Nolet, D., 1987, Seismic tomography: D. Reidel Publ. Co..
Nur, A., and G. Simmons, 1969, The effect of saturation on velocity in low porosity rocks: Earth and Planetary Science Letters, **7**, 183–193.
O'Connell, R. J., and B. Budiansky, 1974, Seismic velocities in dry and saturated cracked solids: Journal of Geophysical Research, **79**, 5412–5426.
Paige, C. C., and M. A. Saunders, 1982, LSQR: An algorithm for sparse linear equations and sparse least squares: ACM Transactions on Mathematical Software, **8**, 43–71.
Plafker, G., G. E. Ericksen, and J. Fernandes Concha, 1971, Geological aspects of the May, 31, 1970 Peru earthquake: Bulletin of the Seismological Society of America, **61**, 543–578.
Podvin, P., and I. Lecomte, 1991, Finite-difference computation of traveltimes in very contrasted velocity models: A massively parallel approach and its associated tools: Geophysical Journal International, **105**, 271–284.
Polymenakos, L., S. Papamarinopoulos, A. Liossis, and C. Koukoli-Chryssanthaki, 2004, Investigation of a monumental Macedonian tumulus by three-dimensional seismic tomography: Archaeological Prospection, **11**, 145–158.
Satori, M., F. Bailifard, M. Jaboyedoff, and J.-D. Roullier, 2003, Kinematics of the 1991 Randa rockslides (Valais, Switzerland): Natural Hazards and Earth System Sciences, **3**, 423–433.
Schindler, C., Y. Cuénod, T. Eisenlohr, and C.-L. Joris, 1993, Die Ereignisse vom 18. April und 9. Mai 1991 bei Randa (VS) — Ein atypischer Bergsturz in Raten (The April 18 and May 9 events near Randa — An atypical sequential rockfall): Eclogae Geologicae Helvetiae, **86/3**, 643–665.
Schmutz, M., Y. Albouy, R. Guérin, O. Maquaire, J. Vassal, J.-J. Schott, and M. Descloîtres, 2000, Joint electrical and time domain electromagnetism (TDEM) data inversion applied to the Super Sauze earthflow (France): Surveys in Geophysics, **21**, 371–390.
Simmons, G., T. Todd, and W. S. Baldridge, 1975, Toward a quantitative relationship between elastic properties and cracks in low porosity rocks: American Journal of Science, **275**, 318–345.
Spillmann, T., H. R. Maurer, H. Willenberg, K. F. Evans, B. Heincke, and A. G. Green, 2006, Characterization of an unstable rock mass based on borehole logs and diverse borehole radar data: Journal of Applied Geophysics, ⟨http://www.sciencedirect.com/science⟩.
Walsh, J. B., 1965, The effect of cracks on the compressibility of rock: Journal of Geophysical Research, **70**, 381–389.
Willenberg, H., 2004, Geologic and kinematic model of a complex landslide in crystalline rock (Randa, Switzerland): Ph.D. thesis 15581, Swiss Federal Institute of Technology (ETH) Zurich, ⟨http://e-collection.ethbib.ethz.ch/cgi-bin/show.pl?type=diss&nr=15581⟩.
Willenberg, H., T. Spillmann, E. Eberhardt, K. Evans, S. Loew, and H. R. Maurer, 2002, Multidisciplinary monitoring of progressive failure processes in brittle rock slopes — Concepts and system design: 1st European Conference on Landslides, Expanded Abstracts, 477–483.